Ammonia Borane All-In-One Modification Strategy Enables High-Performance Perovskite Solar Cells

Jiaxin Ma[1,2], Cong Shao[1,2], Yirong Wang[2,3], Guosheng Niu[1,2], Kaiyi Yang[1,2], Yao Zhao[4], Fuyi Wang[2,4], Zongxiu Nie[2,4], Jizheng Wang[1,2] ✉

HIGHLIGHTS

- An all-in-one modification strategy was developed by introducing a multifunctional complex ammonia borane (BNH_6) into the buried and upper interfaces simultaneously.

- BNH_6 uniquely realizes dual-interfacial defect passivation and iodide oxidation suppression by interacting with SnO_2 through hydrolysis, coordinating with Pb^{2+} and inhibiting the oxidation of I^-.

- The optimized perovskite solar cells achieve a champion efficiency of 26.43% (certified, 25.98%) with negligible current density–voltage hysteresis and significantly improved thermal and light stability.

ABSTRACT Perovskite solar cells have achieved remarkable progress in photovoltaic efficiency. However, interfacial defects at the buried and upper interfaces of perovskite layer remain a critical challenge, leading to charge recombination, ion migration, and iodine oxidation. To address this, we propose a novel all-in-one modification strategy employing ammonia borane (BNH_6) as a multifunctional complex. By incorporating BNH_6 at both buried and upper interfaces simultaneously, we achieve dual-interfacial defect passivation and iodide oxidation suppression through three key mechanisms: (1) hydrolysis-induced interaction with SnO_2, (2) coordination with Pb^{2+}, and (3) inhibition of I^- oxidation. This approach significantly enhances device performance, yielding a champion power conversion efficiency (PCE) of 26.43% (certified 25.98%). Furthermore, the unencapsulated device demonstrates prominent enhanced operation stability, maintaining 90% of its initial PCE after 500 h under continuous illumination. Notably, our strategy eliminates the need for separate interface treatments, streamlining fabrication and offering a scalable route toward high-performance perovskite photovoltaics.
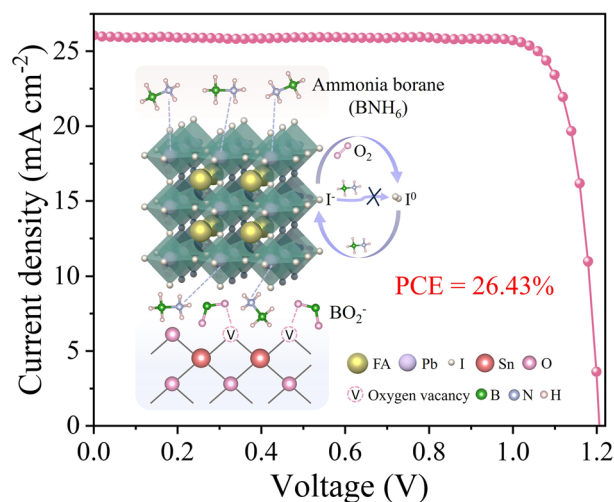
KEYWORDS Ammonia borane; All-in-one modification; Multifunctional complex; Perovskite solar cells

✉ Jizheng Wang, jizheng@iccas.ac.cn

1 Beijing National Laboratory for Molecular Sciences CAS Key Laboratory of Organic Solids, Institute of Chemistry, Chinese Academy of Sciences, Beijing 100190, People's Republic of China

2 School of Chemical Sciences, University of Chinese Academy of Sciences, Beijing 100049, People's Republic of China

3 CAS Key Laboratory of Engineering Plastics, Institute of Chemistry, Chinese Academy of Sciences, Beijing, People's Republic of China

4 Beijing National Laboratory for Molecular Sciences, National Centre for Mass Spectrometry in Beijing, CAS Key Laboratory of Analytical Chemistry for Living Biosystems, Chinese Academy of Sciences, Beijing, People's Republic of China

1 Introduction

Organic–inorganic hybrid perovskite solar cells (PSCs) have become one of the most attractive fields due to their excellent optoelectronic properties [1–5]. The power conversion efficiency (PCE) of PSCs has rapidly reached 27.0% in the past few years [6–8]. This continuous progress is attributed to various attempts, including bandgap modulation [9–11], crystallization behavior regulation [12–17], and interface modification [18–27]. The low-temperature solution method is prevalent for preparing state-of-the-art PSCs. However, perovskite films prepared through such rapid low-temperature approach are liable to generate large numbers of interfacial defects, which serve as nonradiative recombination centers to hinder charge transport [28–31]. To address this, various strategies have been explored. For example, Yi et al. employed 1-[3-(Trimethoxysilyl)propyl]urea (TMPU) at SnO$_2$/perovskite interface and trimethoxy (3,3,3-trifluoropropyl)silane (TMFS) at perovskite/Spiro-OMeTAD interface to passivate detrimental interface defects and facilitate faster carrier extraction [32]. Zheng et al. reported a strategy to dense the hole transport layer (HTL) by introducing (aminomethyl)phosphonic acid (AMP) into the precursor solution, concurrently modifying the top surface of the perovskite with 2-(3-fluorophenyl)ethylamine iodide (mF-PEAI) and piperazinium diiodide (PDI) [33]. These effective interface modification strategies are summarized in Table S1. However, the applying of excessive types of additives is unfavorable to the rapid device manufacturing, as well as the commercial fabrication.

Besides, iodide ions (I$^-$) in the perovskite layer can migrate under the influence of environmental factors due to their lower formation energy [34]. This migration can lead to an uneven ion distribution at the interfaces, and the accumulation of iodine ions at the interfaces may induce adverse redox reactions, which frequently involve the generation of iodine defects (I^0) [35–37]. I^0 is volatile and can easily escape from the perovskite layer, accelerating the degradation of perovskite. Nevertheless, only a few additives were used to address this issue, such as benzylhydrazine hydrochloride (BHC) [38], the redox pairs of Eu^{3+}-Eu^{2+} [35], and fluoroN,N,N″,N″-tetramethylformamidinium hexafluorophosphate (TFFH) [39], serving as reducing agents effectively reduced I^0 back to I$^-$. In spite of these attempts have been made in improving the performance of PSCs,

these works are all achieved by improving the stability of perovskite precursor solutions. However, when perovskite film is exposed to ambient environment, I$^-$ at the interface is more likely to be oxidized and result in defects, making the elimination of interface defects still challenging.

In this work, an all-in-one modification strategy was developed to address these issues. This strategy is achieved by incorporating ammonia borane (BNH$_6$) into the buried (SnO$_2$/BNH$_6$) and upper (PVK/BNH$_6$) interfaces of perovskite layer, respectively (Fig. 1a) to realize dual-interfacial defect passivation and iodide oxidation suppression. BNH$_6$ is a unique molecular complex composed of electron-rich nitrogen elements and electron-poor boron elements that determine its multifunctionality. BNH$_6$ enables the interaction with SnO$_2$ through hydrolysis, passivates the uncoordinated Pb^{2+} to realize dual-interfacial optimization, and acts as a reducing agent to reduce I^0 back to I$^-$ to inhibit iodide oxidation (Fig. 1b). These unique properties enable BNH$_6$ to play an effective role under different treatment conditions (Fig. 1c). Consequently, a typical n-i-p PSC (Fig. 1d) with BNH$_6$ all-in-one modification achieved a champion efficiency of 26.43% (certified, 25.98%) with negligible current density−voltage (J−V) hysteresis. Furthermore, the unencapsulated device demonstrates prominent enhanced operation stability, maintaining 90% of its initial PCE after 500 h under continuous illumination. This work presents a simple and highly effective strategy to address dual-interface defects in perovskite films and eliminate the complexity of multi-additive systems, offering a promising pathway to enhance the compatibility with rapid manufacturing and commercialization.

2 Experimental Section

2.1 Materials

All the chemicals were purchased from commercial vendors without further purification. SnO$_2$ colloid precursor (tin (IV) oxide, 15% in H$_2$O), N,N-dimethylformamide (DMF, 99.8%) and dimethyl sulfoxide (DMSO, 99.8%) were purchased from Alfa Aesar. Chlorobenzene (99.8%) and isopropanol (99.5%) were purchased from Sigma-Aldrich. Acetonitrile (99.9%) was purchased from Acros. CsI (99.999%) was purchased from Sigma-Aldrich. PbI$_2$ (99.999%), FAI (99.9%) and MACl (99.9%) were purchased from Advanced Election Technology Co., Ltd.
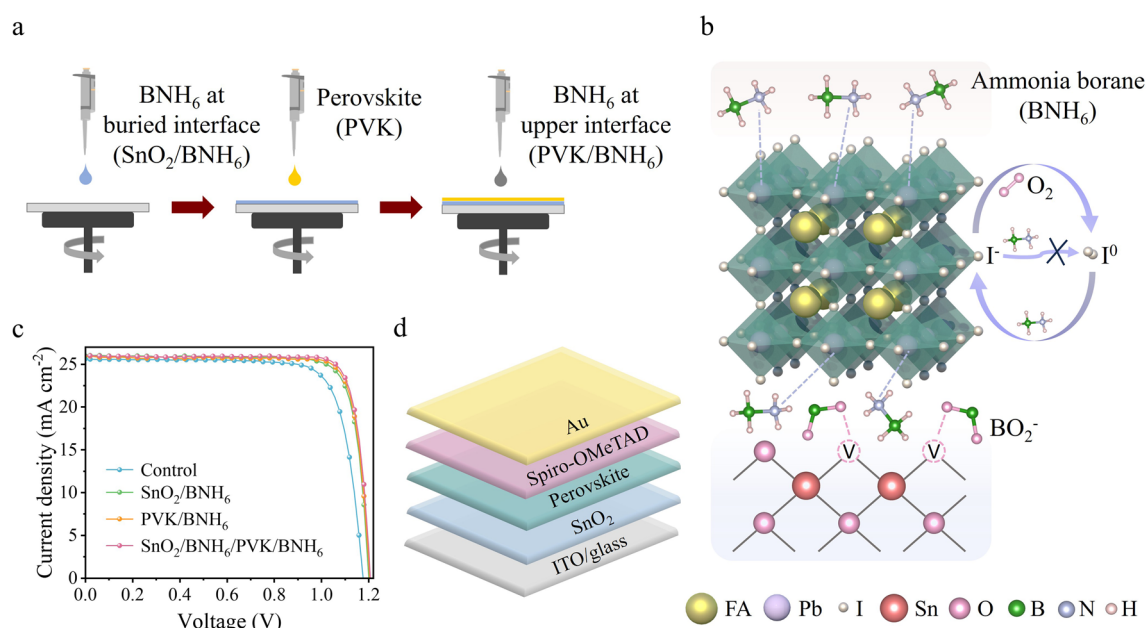
Fig. 1 Structure and preparation of BNH_6 in perovskites. **a** Schematic of device fabrication processes. SnO_2/BNH_6 and PVK/BNH_6 are defined as BNH_6 at the buried and upper interfaces of perovskite layer, respectively. **b** Mechanism diagram of BNH_6 modification at different positions. **c** $J-V$ curves of PSCs under various BNH_6 treatment conditions. **d** Device structure diagram of a typical *n-i-p* PSC

MeO-PEAI (99%), Spiro-OMeTAD (99.9%), 4-tert-butyl-pyridine (96%) and LiTFSI (99%) were purchased from Xi'an Polymer Light Technology. Ammonia borane was purchased from Aladdin Bio-Chem Technology Co., Ltd.

2.2 Solution Preparation

Tin (IV) oxide colloid solution (15 wt%) was diluted with deionized water (volume ratio: 1:2). The BNH_6 solution (1 mg mL^{-1}) coated at the buried interface of perovskite was prepared by dissolving 1.0 mg BNH_6 in 1 mL deionized water. For the $Cs_{0.05}FA_{0.95}PbI_3$ precursor solution, 1.4 M FAI, 0.07 M CsI, 1.58 M PbI_2 and 0.49 M MACl were mixed in the solvent of DMF and DMSO (volume ratio: 8:1) and stirred at room temperature for 6 h. The BNH_6 solution (1 mg mL^{-1}) coated at the upper interface of perovskite was prepared by dissolving 1.0 mg BNH_6 in 1 mL IPA. The MeO-PEAI solution (3 mg mL^{-1}) was prepared by dissolving 3 mg MeO-PEAI in 1 mL IPA. The Spiro-OMeTAD solution was prepared by dissolving 72.3 mg of Spiro-OMeTAD, 28.8 μL of t-BP, and 35 μL of Li-TFSI solution (260 mg mL^{-1}, in acetonitrile) in 1 mL chlorobenzene.

2.3 Device Fabrication

The ITO substrate was cleaned in deionized water, acetone, and ethanol in sequence, followed by being treated with oxygen plasma for 10 min. Next, the SnO_2 colloid solution was spin-coated onto the substrate at 4000 rpm for 30 s and annealed at 150 °C for 30 min in ambient to form the SnO_2 film. Then the BNH_6 solution (dissolved in deionized water) was spin-coated on the SnO_2 film at 4,000 rpm for 30 s and annealed at 150 °C for 10 min in ambient to form the SnO_2/BNH_6 film. After cooling down, the SnO_2 or SnO_2/BNH_6 films were treated with oxygen plasma (60 W) for 5 min. Then the perovskite solution (60 μL) was spin-coated at 1000 rpm for 10 s and 5000 rpm for 30 s. At 20 s from the last, 700 μL diethyl ether (DEE) as an antisolvent was rapidly dropped onto the substrate. Then the perovskite precursor film was annealed at 120 °C for 1 h under an ambient atmosphere with ~25% RH. After the perovskite film was cooled down, the sample was transferred to a nitrogen-filled glove box for further processing. The BNH_6 solution (dissolved in IPA) was spin-coated on the perovskite film at 4000 rpm for 30 s. Then the MeO-PEAI solution (100 μL) was spin-coated for passivation at 4000 rpm for 30 s. Then the perovskite film was annealed at 100 °C for 5 min. The

Spiro-OMeTAD solution (50 µL) was spin-coated onto the perovskite layer at 4000 rpm for 30 s. Finally, 80 nm Au electrode was deposited by thermal evaporation.

2.4 Density Functional Theory Calculation

Theoretical calculations were performed with the Vienna ab initio simulation package (VASP). The exchange–correlation energy is described by the Perdew-Burke-Ernzerhof (PBE) form of generalized-gradient approximation (GGA) exchange–correlation energy functional. The structure optimizations of systems of BH_3NH_3 before and after adsorption on PbI_2 and FAI terminal $FAPbI_3$ (100) surfaces have been carried out by allowing top layer atomic positions to vary and fixing lattice parameters and bottom layer atomic positions until the energy difference of successive atom configurations was less than 10^{-6} eV. The force on each atom in the relaxed structures was less than 0.015 eV $Å^{-1}$. The cutoff energy for the plane-wave basis set was set to 400 eV. The k-point spacing was set to be smaller than 0.03 $Å^{-1}$ over Brillouin zone (BZ).

2.5 Measurements

The current density – voltage ($J - V$) characteristics of the devices were measured using a Keithley 2420 under AM 1.5 sunlight at an irradiance of 100 mW cm^{-2} provided by a solar simulator (Newport, Oriel Sol3A Class AAA, 94043A). Light intensity was calibrated using a monocrystalline silicon reference cell with a KG5 window (Newport, Oriel 91,150). The J − V curves were obtained with a scan rate of 100 mV s^{-1} and a scan step of 20 mV from 1.22 to 0.00 V (reverse) or from 0.00 to 1.22 V (forward). The area of the cell is 0.1225 cm^2 and a mask of 0.09881 cm^2 (certificated by NIM, China. The certificate No.: CDjc2023 − 08390) was used to determine the effective area of the device before the test. Heating acceleration: Unencapsulated devices were heated at 65 ± 3 °C in a nitrogen atmosphere (ISOS-T-1). Long-term light stability tests: Unencapsulated devices were treated by white light-emitting diode (LED) with an intensity of 100 mW cm^{-2} at 23 ± 3 °C in a nitrogen atmosphere (ISOS-L-1). EQE measurements were recorded by an Enli Technology EQE system, which was calibrated by a certified silicon solar cell. The scan interval was 5 nm, and there was no bias light and mask used during the measurement. The top-view and cross-sectional SEM images were obtained using Hitachi S-4800

at the accelerating voltage of 5.0 kV. The surface roughness of perovskite film was measured by an AFM (Nanoscope V, Vecco) in tapping mode under the ambient atmosphere. The XRD patterns were taken on PANalytical Empyrean with a Cu Kα radiation ($\lambda = 1.5406$ Å) and a scanning rate of 5° min^{-1} in the 2θ range of 5°–50° at a step size of 0.02 s. 2D-XRD spectra were measured using a Rigaku SmartLab X-ray diffractometer with Cu Kα1 (1.54060 Å) and a HyPix-3000 2D hybrid pixel array detector. All samples for XRD testing were prepared on quartz glass substrates. The steady PL spectra was recorded by Horiba FluoroMax + fluorescence spectrometer with an excitation at 490 nm. Time-resolved PL was carried out by the FLS980 fluorescence spectrometer with excitation wavelength at 485 nm. ToF–SIMS profiling measured the depth distributions of the negative ions with perovskite on the ITO substrate. The samples were analyzed using a ToF–SIMS 5 instrument (IONTOF) with a Bi + primary beam (10 keV and 1 pA) and Cs + sputter beam (3 keV and 5 nA). The sputter size was 100 µm × 100 µm. The UV absorption spectra of perovskite films and FAI solutions were measured using a Hitachi U3900 spectrophotometer. XPS/UPS measurements were obtained using an XPS/UPS system (ESCALAB250XI, Thermo Fisher Scientific). LEIPS measurement was performed on a customized ULVAC-PHI LEIPS instrument with Bremsstrahlung isochromatic mode. FTIR were performed on a HITACHI F-4500IR spectrometer with samples prepared as KBr tablets. The mass ratio of the sample to KBr is 1:100. Raman spectra were recorded using an NT-MDT NTEGRA Spectra system. EIS and M-S tests were measured with an electrochemical workstation (Modulab XM, USA). ^{1}H NMR spectra were recorded on a Bruker Avance 400 Spectrometer. The concentration of the sample is 10 mg mL^{-1} in DMSO-d_6.

2.6 Calculation Methods

2.6.1 Conductivity and Electron Mobility

The conductivity (σ) was calculated using Eq. (1):

$$\sigma = \frac{I}{V} \tag{1}$$

where I is the current, V is the voltage.

The electron mobility (μ_e) was calculated using Eq. (2):

$$J = \frac{9}{8}\varepsilon\varepsilon_0\mu\frac{V^2}{L^3} \tag{2}$$

where J is the current density, ε is the relative dielectric constant, ε_0 is vacuum permittivity, V is the voltage, and L is the film thickness.

2.6.2 Residual Stress

The residual stress (σ) was calculated using Eq. (3):

$$\sigma = -\frac{E}{2(1+v)}\frac{\pi}{180°}\cot\theta_0\frac{\partial(2\theta)}{\partial(\sin^2\psi)} \tag{3}$$

where E is the perovskite modulus (10 GPa), and v is the Poisson's ratio of perovskite (0.3).

2.6.3 Ideality Factor

The diode ideality factor (n) was determined by fitting V_{oc} as a function of light intensity using Eq. (4):

$$V_{oc} = \frac{nkT\ln(I_{light})}{q} + C \tag{4}$$

where n represents the ideality factor to single-molecule recombination, I_{light} is the light intensity, k is Boltzmann's constant, T is temperature, and q is the elementary charge.

3 Results and Discussion

3.1 Interaction Between BNH_6 and SnO_2

The hydrolysis characteristic of BNH_6 leads to the production of BO_2^- (Fig. S1) [40], which can interact with SnO_2. To further investigate the interaction between BNH_6 and SnO_2, X-ray photoelectron spectroscopy (XPS) was carried out for the SnO_2 film (SnO_2) and BNH_6 treated SnO_2 film (SnO_2/BNH_6). In the N 1s spectra (Fig. 2a), the peaks around 403 eV originate from molecular N_2 adsorbed on the surface of SnO_2, and the occurrence of NH_x around 399 eV in the SnO_2/BNH_6 film confirms that BNH_6 was successfully introduced and hydrolyzed to produce NH_4^+ during annealing process. In the B 1s spectra (Fig. 2b), the signal of the SnO_2/BNH_6 film can be divided into three peaks. The peak around 192.1, 191.6, and 191.0 eV represents the B–O peak, B–N peak and B–H peak, respectively. To investigate the proportion of BO_2^- produced by hydrolysis of BNH_6, the value obtained by the integrated areas ratio of $S_{B–O}/(S_{B–O} + S_{B–N} + S_{B–H})$ is 30%, indicating that 30% of BNH_6 molecules hydrolyze to produce BO_2^-. Besides,

the above results indicate that most BNH_6 molecules are not hydrolyzed and still exist in the form of B–N and B–H bonds, which will be beneficial for the subsequent film formation and defects passivation of perovskite. The Sn 3d peaks at 486.4 and 494.8 eV for the SnO_2 film shift to 486.1 and 494.5 eV for the SnO_2/BNH_6 film, respectively, which indicates the electron density increased after BNH_6 treated owing to the negative charge on BO_2^- (Fig. 2c). As revealed by O 1s spectra (Fig. 2d), the signals of the SnO_2 and SnO_2/BNH_6 films can be fitted into three peaks. The peak at about 530 eV is assigned to the lattice oxygen (M–O), representing the fully coordinated oxygen atoms within the SnO_2 crystal lattice. The peak at about 531 eV is attributed to oxygen vacancies (O_{vac}), which is associated with defect-related states. And the peak at about 532 eV corresponds to surface hydroxyl groups or adsorbed water [41, 42]. It is easily found that the relative intensities of M–O increased (from 44% to 61%), as well as O_{vac} (from 34% to 19%) and H–O (from 22% to 20%) decreased after BNH_6 modification, indicating suppressed nonradiative recombination and enhanced electron mobility [43], which is attributed to the occupation of BO_2^- on O_{vac} (Fig. 2e). In addition, during the actual device fabrication process, the O 1s XPS spectra of SnO_2 and SnO_2/BNH_6 films treated by oxygen plasma exhibit higher M–O relative intensity and lower O_{vac} and H–O relative intensities compared to the untreated films (Fig. S2). Correspondingly, the performance of the resulting devices is also enhanced (Fig. S3 and Table S2). These features suggest a strong interaction between BNH_6 and SnO_2 due to the hydrolysis product of BNH_6 (BO_2^-), interacting with the uncoordinated Sn^{4+} by filling O_V through adsorption. In addition, the SnO_2 and SnO_2/BNH_6 films were subjected to X-ray diffraction (XRD) characterization. As shown in Fig. S4, the position and diffraction intensity of peaks are almost the same after BNH_6 modification, illustrating that BNH_6 does not damage the structure of the pristine SnO_2.

To investigate the energy band structure of the SnO_2 and SnO_2/BNH_6 films, ultraviolet photoelectron spectroscopy (UPS) and low energy inverse photoemission spectroscopy (LEIPS) were carried out. As shown in Fig. S5, the secondary electron cutoff edges (E_{cutoff}) shifts from 16.72 to 16.82 eV after BNH_6 modification, resulting in a decrease work function from 4.50 to 4.40 eV. Meanwhile, the conduction band (E_C) shifts from − 4.44 to − 4.29 eV after the introduction of BNH_6 (Fig. S6). The better matching of energy levels with perovskite for SnO_2/BNH_6 is expected
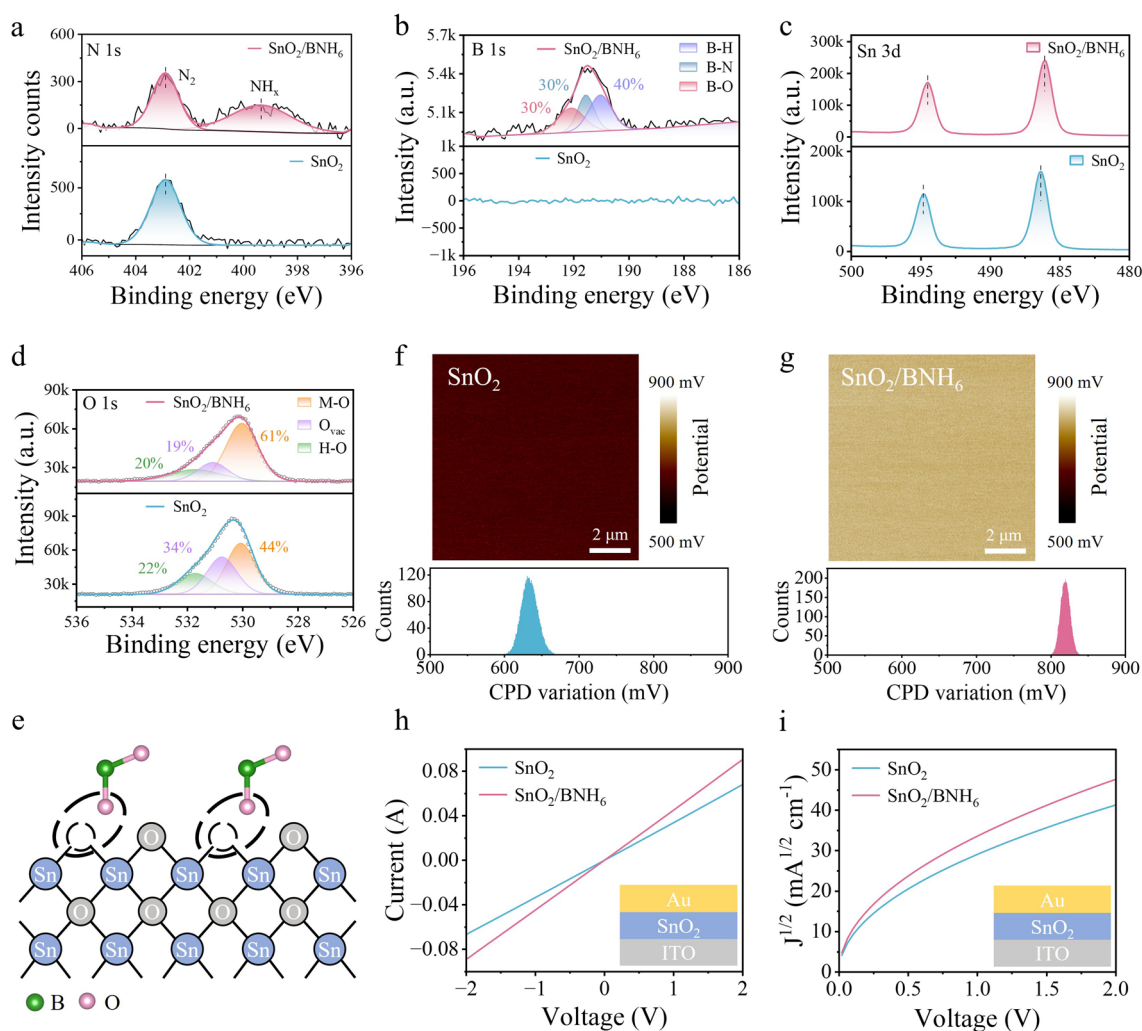
Fig. 2 Interaction between BNH_6 and SnO_2. **a** N 1s, **b** B 1s, **c** Sn 3d, **d** O 1s XPS spectra of the SnO_2 and SnO_2/BNH_6 films. **e** Schematic illustration of the occupation of BO_2^- on O_V. KPFM images of the **f** SnO_2 film and **g** SnO_2/BNH_6 film. The statistical potential distributions of film surfaces are shown at the bottom. CPD, contact potential difference. **h** The electrical conductivity and **i** the electron mobility of the SnO_2 and SnO_2/BNH_6 films. Inset shows the architecture of devices

to reduce interface energy barrier and thus suppress interface recombination. Then Kelvin probe force microscopy (KPFM) was measured to study the electrical charge distribution on the film surface, with contact potential difference (CPD) spectra shown in Fig. 2f, g. The SnO_2/BNH_6 film showed a higher CPD (819 mV) compared with the SnO_2 film (634 mV), indicating a decrease in the work function and an increase of the Fermi level, which is consistent with the result of UPS.

In addition, the transmittance of SnO_2 layer coated on indium doped tin oxide (ITO) glass is not affected with BNH_6 modification (Fig. S7). And the absorption edge of SnO_2 nearly does not change after BNH_6 modified (Fig.

S8). The conductivity of the SnO_2/BNH_6 film (3.37×10^{-3} mS cm^{-1}) is significantly higher than that of the SnO_2 film (2.53×10^{-3} mS cm^{-1}) (Fig. 2h), and the electron mobility of the SnO_2/BNH_6 film (3.18×10^{-3} cm^2 V^{-1} S^{-1}) is also greater than that of the SnO_2 film (2.43×10^{-3} cm^2 V^{-1} S^{-1}) (Fig. 2i). The enhanced charge transport provides preferable electron diffusion and charge extraction, achieving higher open circuit voltage (V_{OC}) and fill factor (FF) of PSCs. The atomic force microscope (AFM) measurement was carried out to study the root mean square (RMS), which is 1.21 and 0.80 nm for the SnO_2 and SnO_2/BNH_6 films, respectively (Fig. S9). The reduced roughness of the SnO_2/BNH_6 film is attributed to the reduction in O_V, which is conducive to
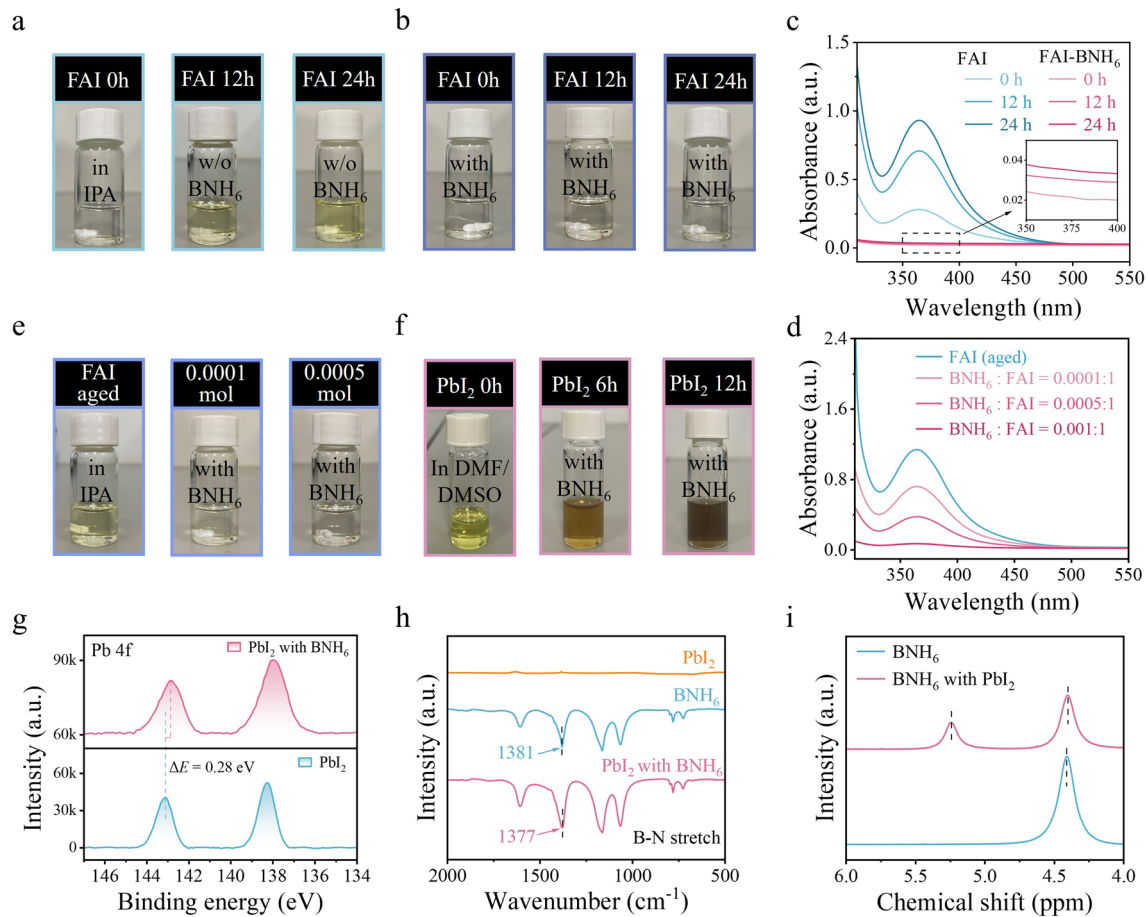
Fig. 3 Interaction between BNH_6 and FAI/PbI_2. **a** The color change process of fresh FAI solution without BNH_6 additive after ambient aging. **b** The color change process of fresh FAI solution with BNH_6 additive after ambient aging. **c** UV–vis absorption spectra of fresh FAI solution with and without BNH_6 after ambient aging. **d** UV–vis absorption spectra of aged FAI solution after introducing different concentrations of BNH_6. **e** The color change process of aged FAI solution after introducing different concentrations of BNH_6. **f** The color change process of PbI_2 solution with BNH_6 after ambient aging. **g** Pb 4f XPS spectra of PbI_2 powders with and without BNH_6. **h** FTIR spectra of PbI_2, BNH_6, and PbI_2 with BNH_6 films. **i** ^{1}H NMR spectra of BNH_6 and BNH_6 with PbI_2

facilitating optimal contact with perovskite film [44]. Additionally, the contact angle of the SnO_2/BNH_6 film (4.8°), is obviously smaller than that of the SnO_2 film (7.2°), measuring by dropping perovskite precursor solution on the SnO_2 and SnO_2/BNH_6 films, respectively (Fig. S10). The improved wettability indicates the better coverage for perovskite, which is consistent with the RMS results.

3.2 Interaction Between BNH_6 and FAI/PbI_2

The reaction between I^- and O_2 has a thermodynamic tendency when the perovskite precursor solution is exposed

to air, leading to the degradation of the precursor solution, thus seriously affecting the performance of devices [38]. Meanwhile, the depletion of I^- generates iodine interstitials accessibly, which is prone to form deep trapping states, causing more nonradiative recombination. To address this issue, BNH_6 is applied and its function can be expressed by Fig. S11. We first attempted to mix BNH_6 (0.001 mol) and FAI (1 mol) in 1 mL DMF to investigate the interaction between BNH_6 and FAI. After continuous stirring along with 60 °C heating and air exposure, the transparent FAI solution without BNH_6 turned to light yellow after 12 h aging and became bright yellow after 24 h aging (Fig. 3a). An absorption peak at 365 nm in the

ultraviolet visible absorption spectroscopy (UV–vis) spectra gradually increased with aging time (Fig. 3c), which is ascribed to the oxidation of I^- into I^0. Surprisingly, the color of FAI solution mixed with BNH_6 remained transparent after 24 h aging (Fig. 3b), which is consistent with the result of almost no peak at 365 nm in the UV–vis spectra (Fig. 3c), demonstrating BNH_6 can suppress the oxidation from I^- to I^0. Importantly, yellow returned to transparent when BNH_6 with increased concentrations were added to the aged FAI solution, accompanied by a notable reduction in the absorption peak observed at 365 nm (Fig. 3d, e). This result proves that the formed I^0 can be reduced to I^- with the BNH_6 addition. To further quantitatively demonstrate the effectiveness of BNH_6 in inhibiting I^- oxidation, we have supplemented ion chromatography (IC) measurements. Specifically, we dissolved 8 mg of FAI in 100 mL of deionized water at ambient conditions and monitored the concentration of I^- at different aging times. As shown in Fig. S12, the I^- concentration gradually decreased with time, indicating progressive oxidation of I^- to I_2. In contrast, after adding BNH_6 to the solution, the I^- concentration remained almost unchanged over the same aging period, and was significantly higher than that in the control sample without BNH_6. After 72 h, the I^- concentration in the sample without BNH_6 decreased by 5.0%, while the I^- concentration in the sample with BNH_6 addition decreased by only 0.7%. These results provide clear and quantitative evidence that BNH_6 can effectively suppress the oxidation of I^- and thus mitigate the formation of elemental iodine. The reducibility of BNH_6 is due to the H atom connected to the B atom can lose electrons and be oxidized to H_2. The chemical reaction equation for BNH_6 reducing I^0 to I^- is speculated as follows:

$$2NH_3 \cdot BH_3 + 2I^0 \rightarrow 2NH_3 \cdot BH_2I + H_2 \tag{5}$$

To explore the coordination between BNH_6 and Pb–I framework, density functional theory (DFT) was employed to calculate the adsorption energies of BNH_6 on the surface of $FAPbI_3$ both with PbI_2 and FAI terminations (Fig. S13). DFT calculations show that BNH_6 is likely to bind to the FAI−terminated surface more stable with the adsorption energy of − 2.15 eV compared with the PbI_2-terminated surface with the adsorption energy of − 1.03 eV.

Then BNH_6 was added to PbI_2 solution resulted in a noticeable color change after stirring for 6 h at room temperature. The color of the solution deepened significantly after 12 h (Fig. 3f) while the pristine PbI_2 solution displayed no obvious alteration (Fig. S14), which is derived from the coordination between the N atom in BNH_6 and Pb^{2+}. To further testify this coordination, XPS, Fourier transform infrared spectroscopy (FTIR) and ^{1}H nuclear magnetic resonance (NMR) were employed. In the XPS spectra (Fig. 3g), the Pb 4f peaks of PbI_2 powders shift to lower binding energy after the introduction of BNH_6, which is originated from the electron transfer from BNH_6 to Pb^{2+}, indicating the coordination of Pb–N. Additionally, FTIR analysis revealed shifts in the stretching vibration peaks of N–H (Fig. S15) and B–N (Fig. 3h) after mixing with PbI_2, suggesting potential coordination interactions between BNH_6 and Pb^{2+}. Furthermore, in the ^{1}H NMR spectra (Fig. 3i), the peak at 4.41 ppm, corresponding to the H atoms connected to B atoms in pure BNH_6, splits into two peaks at 5.24 and 4.40 ppm upon the addition of PbI_2. This shift suggests a strong interaction between BNH_6 and PbI_2, which alters the chemical environments of the H atoms in the BH_3 group. This behavior is likely due to the breaking of B–N bonds in some BNH_6 molecules allowing the N atom with lone pair electrons to coordinate with Pb^{2+} [45–47]. To quantify the extent of B–N bond breakage in BNH_6 molecules during interaction with Pb^{2+} from the ^{1}H NMR spectra, the following formula was applied:

$$BNH_6 \text{ breakage}\% = \frac{S_{Pb-N}}{S_{Pb-N} + S_{B-N}} \tag{6}$$

where S_{Pb-N} represents the integrated area of the Pb–N peak, and S_{B-N} represents the integrated area of the B–N peak. The calculation result suggests that 29% of BNH_6 molecules can additionally coordinate with Pb^{2+}.

3.3 Film Characterization

The morphology of perovskite films with and without BNH_6 modification was investigated by scanning electron microscopy (SEM) and atomic force microscopy (AFM). SEM images (Fig. 4a–d) show that the perovskite film with BHN_6 buried modification (SnO_2/BNH_6/PVK) exhibits significantly much larger grain size, indicating that BNH_6 positively affects the crystallization of perovskite. While the grain size of the perovskite film with BNH_6 upper modification (SnO_2/PVK/BNH_6) does not increase significantly. This
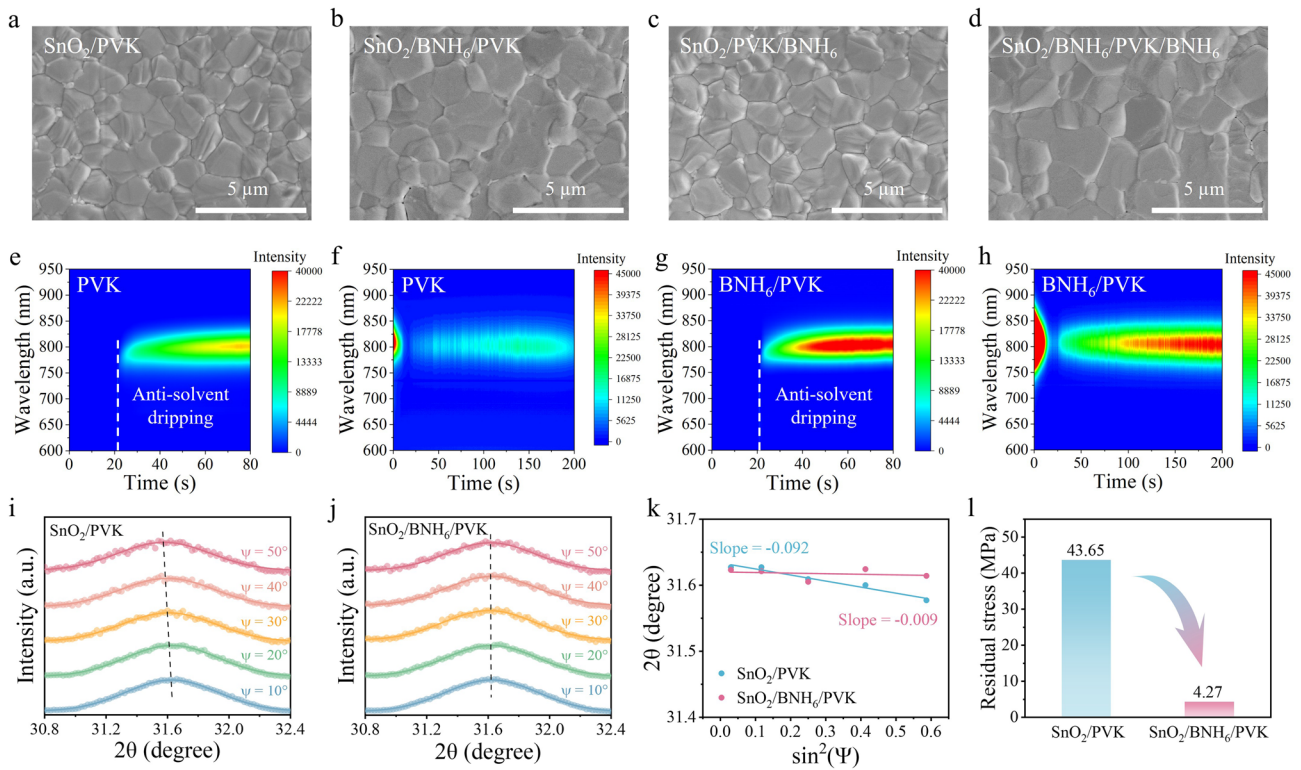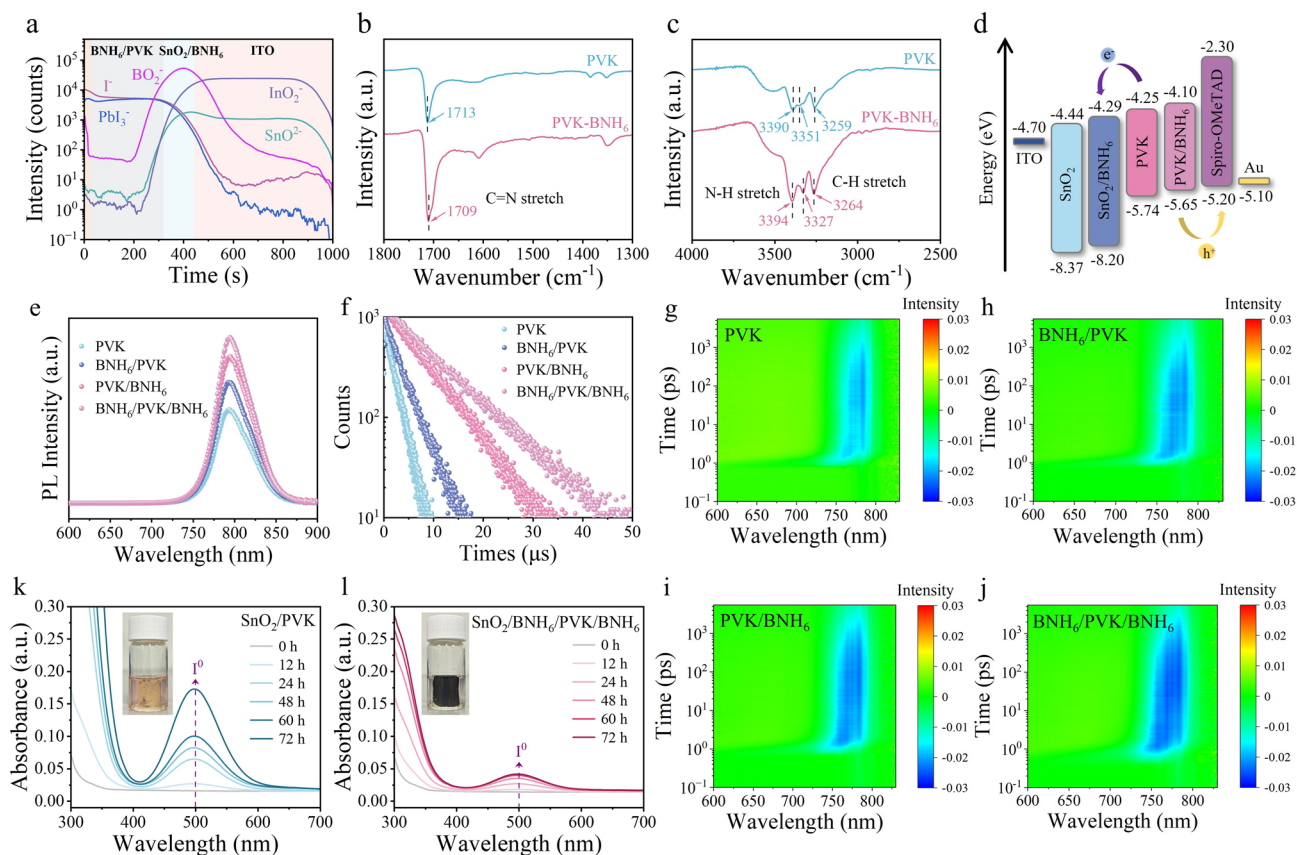
Fig. 4 Characteristics of perovskite films. SEM images of **a** SnO$_2$/PVK, **b** SnO$_2$/BNH$_6$/PVK, **c** SnO$_2$/PVK/BNH$_6$ and **d** SnO$_2$/BNH$_6$/PVK/BNH$_6$ films. In situ PL spectra of the PVK film during the **e** spin-coating and **f** annealing process. In situ PL spectra of the BNH$_6$/PVK film during the **g** spin-coating and **h** annealing process. GIXRD spectra at different Ψ angles (from 10° to 50°) of **i** SnO$_2$/PVK and **j** SnO$_2$/BNH$_6$/PVK films. **k** Linear fit of 2θ–$\sin^2\psi$ for the SnO$_2$/PVK and SnO$_2$/BNH$_6$/PVK films. **l** Comparison of residual stress of the SnO$_2$/PVK and SnO$_2$/BNH$_6$/PVK films

is because BNH$_6$ mainly plays the role of passivating Pb^{2+} and reducing I^0 at the upper interface rather than regulating crystallization. The grain-size distributions of these films are displayed in Fig. S16. The pristine perovskite (SnO$_2$/PVK) film has an average grain size of 1.59 µm, while the SnO$_2$/BNH$_6$/PVK, SnO$_2$/PVK/BNH$_6$ and the dual-interface modified (SnO$_2$/BNH$_6$/PVK/BNH$_6$) films reveal larger size of 2.26, 1.70, and 2.15 µm, respectively. Meanwhile, the root mean square (RMS) roughness of SnO$_2$/PVK film measured by AFM (Fig. S17) is 27.8 nm, and the reduced roughness in the SnO$_2$/BNH$_6$/PVK (23.5 nm), SnO$_2$/PVK/BNH$_6$ (24.7 nm) and SnO$_2$/BNH$_6$/PVK/BNH$_6$ (19.0 nm) films is beneficial for defects suppression and charge extraction [47].

2D X-ray diffraction (2D-XRD) was conducted to explore the crystallization of perovskite film with and without BNH$_6$ modification (Fig. S18). The results show that the (001) and (002) crystal planes of α-FAPbI$_3$ are aligned parallel to the substrate normal, with no noticeable change across all the samples. Besides, the diffraction peaks of (001) and

(002) crystal planes significantly enhanced for the SnO$_2$/BNH$_6$/PVK film, while no obvious changes are found for the SnO$_2$/PVK/BNH$_6$ film. The same phenomenon is observed from XRD patterns (Fig. S19). By comparison, the SnO$_2$/BNH$_6$/PVK/BNH$_6$ film exhibits better crystal orientation of α-FAPbI$_3$ for facilitating charge transfer. To further clarify the impact of BNH$_6$ modification on the crystallization of perovskite, in situ photoluminescence (PL) measurement was performed during perovskite fabrication process. Figure 4e–h depicts the in situ PL spectra of perovskite films during spin coating and thermal annealing processes. During the spin coating stage, the BNH$_6$/PVK film displays a stronger PL intensity in a shorter time upon anti-solvent dripping (Fig. 4e, g), implying the faster nucleation of α-FAPbI$_3$ for the BNH$_6$/PVK film [48, 49]. During the thermal annealing process (Fig. 4f, h), rapidly increasing PL intensities of the both films arise due to the generation of α-FAPbI$_3$, and the subsequent sharp decrease can be mainly attributed to solvent volatilization and crystallization

Fig. 5 Characteristics of perovskite films. **a** ToF–SIMS depth profiles of I^-, PbI_3^-, InO_2^-, SnO^{2-} and BO_2^- for ITO/SnO$_2$/BNH$_6$/PVK/BNH$_6$. **b, c** FTIR spectra of the PVK and PVK-BNH$_6$ films. **d** The schematic diagram of the energy level arrangement of the components with and without BNH$_6$. **e** PL and **f** TRPL spectra of the PVK, BNH$_6$/PVK, PVK/BNH$_6$ and BNH$_6$/PVK/BNH$_6$ films. Characteristic pseudo-color TAS plots of the **g** PVK, **h** BNH$_6$/PVK, **i** PVK/BNH$_6$ and **j** BNH$_6$/PVK/BNH$_6$ films. UV–vis spectra of the toluene immersed with the **k** SnO$_2$/PVK and **l** SnO$_2$/BNH$_6$/PVK/BNH$_6$ films under light and heat exposure at different times. Inset photographs are the samples after light and heat aging for 72 h

restructuring [50–52]. Then the re-enhanced and gradually stabilized PL intensity exhibits the dissolution–recrystallization equilibrium of α-FAPbI$_3$ on the surface. The PL intensity of the BNH$_6$/PVK film begins to sharply increase at 27 s, later than 19 s of the PVK film, indicating BNH$_6$ effectively slows down the crystal growth. The rapid nucleation and delayed crystal growth of the BNH$_6$/PVK film signifies higher quality perovskite with less nonradiative recombination, which is attributed to the ability of BNH$_6$ to regulate the crystallization of perovskite.

The remarkable improvement in the crystallinity of the perovskite also affects the release of residual stress. Grazing-incidence X-ray diffraction (GIXRD) was investigated at various angles to assess the residual stress in perovskite films. The diffraction peaks of (012) crystal plane for the SnO$_2$/PVK progressively shift to the lower 2θ by varying

ψ from 10° to 50° (Fig. 4i, j), indicating the increase in the crystal plane distance d$_{(012)}$ and the presence of tensile stress in the film. In contrast, the SnO$_2$/BNH$_6$/PVK film exhibits negligible shifts across different angles, suggesting that the d$_{(012)}$ remains nearly constant at different depths of the perovskite film, indicating released residual stress. The slopes of the fitted lines by fitting 2θ as a function of $\sin^2 \psi$ and the residual stress are shown in Fig. 4k, l. The SnO$_2$/BNH$_6$/PVK film exhibited smaller negative slope (− 0.009) and residual stress (4.27 MPa) compared with the negative slope (− 0.092) and residual stress (43.65 MPa) for the SnO$_2$/PVK film, suggesting BNH$_6$ buried modification can significantly release residual tensile stress in perovskite film, which is favorable for the efficiency and stability of PSCs [53].

Time-of-flight secondary-ion mass spectrometry (ToF–SIMS) reveals that the emergence of BO$_2^-$ proves

BNH_6 had been successfully introduced into the buried and the upper interfaces of perovskite film (Fig. 5a). FTIR was then applied to study the interactions between BNH_6 and perovskite. As shown in Fig. 5b, c, the C=N stretching peak shifts from 1713 to 1709 cm^{-1}, the N–H stretching peak shifts from 3390 to 3394 cm^{-1}, and the C–H stretching peak shifts from 3351/3259 to 3327/3264 cm^{-1} on adding BNH_6, suggesting the generation of the hydrogen bonds between BNH_6 and FAI. The interactions between BNH_6 and perovskite were further validated by XPS (Fig. S20). It is found that Pb 4f, I 3d, and N 1s from the PVK/BNH_6 film all exhibit certain red-shift compared to the PVK film, further proving the strong interactions between BNH_6 and FAI/PbI_2. UPS and LEIPS were employed to illustrate the energy band alignment of perovskite with BNH_6 modification. Figure S21 exhibits that BNH_6 treatment decreases the E_{cutoff} from 17.00 to 16.92 eV, resulting in the work function of the perovskite film shifts from 4.22 to 4.30 eV. Meanwhile, the valence band (E_V) calculated from UPS shifts from − 5.74 to − 5.65 eV, and the E_C measured from LEIPS shifts from − 4.25 to − 4.10 eV (Fig. S22), demonstrating better energy alignment between perovskite layer and hole transport layer for extracting holes and blocking electrons (Fig. 5d). UV–vis absorption spectra show that the perovskite films incorporating BNH_6 exhibit stronger absorption compared with the SnO_2/PVK film, with SnO_2/BNH_6/PVK/BNH_6 film exhibiting the strongest absorption, which can be attributed to the enhanced film quality after introducing BNH_6. In addition, the bandgap is determined to be 1.53 eV, which has negligible influence with BNH_6 modification (Fig. S23). Moreover, Urbach energies (E_u) were also compared from UV–vis absorption spectra (Figs. S24 and S25). The lowest E_u of SnO_2/BNH_6/PVK/BNH_6 film represents the highest structural quality during the crystal formation of perovskites [54], which is attributed to the multifunctional role of the BNH_6 molecule in passivating various defects.

Then we recorded photoluminescence (PL), time-resolved photoluminescence (TRPL) and PL mapping to track the film quality and charge recombination dynamics. In order to eliminate the decrease in PL intensity and lifetime caused by SnO_2 as a transport layer [55, 56], we have prepared the PVK, BNH_6/PVK, PVK/BNH_6, BNH_6/PVK/BNH_6 films to explore the role of BNH_6 at the buried and upper interfaces of perovskite. Compared with the

PVK film, the BNH_6/PVK and PVK/BNH_6 films exhibit enhanced intensity of PL and PL mapping (Figs. 5e and S26), as well as the lifetime (Fig. 5f and Table S3), indicating the suppressed nonradiative recombination with BNH_6 passivation. Meanwhile, the BNH_6/PVK/BNH_6 film modified with dual interfaces exhibits the highest intensity of PL and PL mapping, with the lifetime up to 9.1 μs. These results suggest that the BNH_6 all-in-one modification strategy can suppress the defect-induced nonradiative recombination to improve the quality of perovskite. Subsequently, femtosecond transient absorption spectroscopy (fs-TAS) was applied to determine the charge transfer behaviors of the four perovskite films mentioned above. The characteristic pseudo-color TAS plots (Fig. 5g–j) show that the BNH_6/PVK/BNH_6 film exhibits the least faded ground state bleaching (GSB) signal, as well as the strongest GSB peak intensity among the four samples (Fig. S27), which represent the longest carrier lifetime. This result agrees with the lifetimes gained from the GSB decay kinetic of fs-TAS at 783 nm (Fig. S28) [57–60]. The longer carrier lifetime after BNH_6 all-in-one modificated implies the trap state elimination and suppressed nonradiative recombination, which is beneficial for the performance of device.

We further investigated the stability of perovskite films. After immersing the perovskite films into toluene solution while simultaneous exposing them to light exposure and applying 60 °C thermal treatment for 72 h, the control film shows noticeable yellowing and significant degradation. The related toluene solution turns pink as well as a strong I^0 characteristic absorption peak appears at ≈ 500 nm in the UV–vis spectrum (Fig. 5k, l). By comparison, the SnO_2/BNH_6/PVK/BNH_6 film exhibits no significant color change, and the I^0 characteristic absorption peak is much weaker compared to the SnO_2/PVK film, indicating that BHN_6 significantly suppressed the oxidation of I^- to I^0 and the formation of I^0 and V_I defects. In addition, XRD results (Fig. S29) show that after accelerated aging, the I^0 characteristic peak intensity of the control film is much higher than that of the target film, further proving that the improved stability of perovskite films with BNH_6 all-in-one modification, as well as BNH_6 can effectively prevent the oxidation of I^- to I^0 and reduce the formation of related defects.
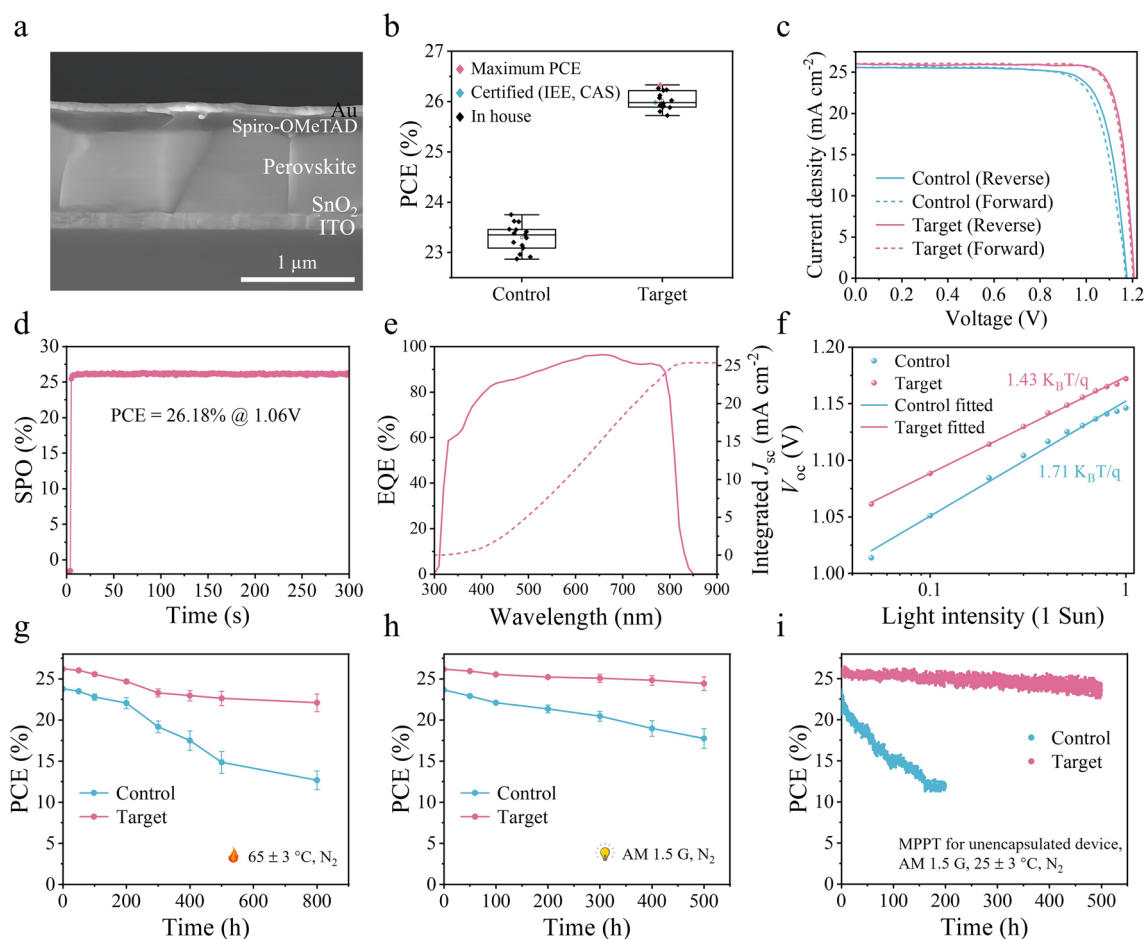
Fig. 6 Performance and stability of the devices. **a** Cross-sectional SEM image of the device structure. **b** Efficiency statistics of both solar cells including the certified value obtained at the Institute of Electrical Engineering Chinese Academy of Sciences (IEE, CAS) and lab measured efficiencies. **c** J−V curves of the control and target devices. **d** SPO curve of the target device. **e** EQE curve and integrated current density of the target device. **f** Dependence of V_{oc} on light intensity of the control and target devices. Long-term stability of the unencapsulated control and target devices stored **g** in glove box with N_2 atmosphere under 65 ± 3 °C heat, **h** in glove box with N_2 atmosphere under AM 1.5 G illumination. **i** MPPT values recorded for the control and target devices with unencapsulation under AM 1.5 G illumination at 25 ± 3 °C with N_2 atmosphere

3.4 Device Performance and Characterization

To evaluate the impact of BNH_6 all-in-one modification strategy on photovoltaic performance, we fabricated a typical *n-i-p* PSC with the architecture of glass/ITO/SnO$_2$/Cs$_{0.05}$FA$_{0.95}$PbI$_3$/Spiro-OMeTAD/Au (Fig. 6a). We recorded the $J-V$ characteristics under simulated 1 sun irradiation with an intensity of 100 mW cm^{-2} (AM 1.5 spectrum). In order to regulate the concentrations of BNH_6 at the buried and upper interfaces of perovskite film separately, we made devices under each condition for comparison, as shown in Fig. S30 and Table S4. After optimization, the best concentrations of BNH_6 are both 1 mg mL^{-1} at the buried and

upper interfaces of perovskite film. Thus, 15 PSCs were prepared under control and target (BNH_6 all-in-one modification) conditions to study the statistical distribution of current density (J_{sc}), V_{oc}, FF and PCE (Figs. 6b and S31). By contrast, the average PCE of target is higher than that of control. In addition, the champion PCE of the target PSCs significantly increases from 23.62% to 26.43% (the pink dot in Fig. 6b), with the V_{oc} of 1.206 V, J_{sc} of 26.05 mA cm^{-2}, and FF of 84.12%, showing a negligible hysteresis (Fig. 6c and Table S5). The significant improvement in PCE can be attributed to the reduction of I^0 related defects and the passivation of the buried and upper interfaces of perovskite film. Some devices were sent to an independent photovoltaic

testing laboratory (Institute of Electrical Engineering, Chinese Academy of Sciences) for certification, with a certified PCE of 25.98% (the blue dot in Fig. 6b, certificate attached in Fig. S32). Additionally, the device exhibits a high stabilized power output (SPO) of 26.18% (biased at 1.06 V), as shown in Fig. 6d. Meanwhile, Fig. 6e shows the external quantum efficiency (EQE) spectrum, with the integrated J_{sc} of 25.36 mA cm^{-2} for the target device, which is closed to the J_{sc} determined from the $J-V$ curves. The analysis of EQE spectrum shows that the bandgap of perovskite is about 1.53 eV (Fig. S33), which is consistent with the bandgap measured from UV–vis absorption spectrum (Fig. S23).

We further utilized space charge-limited current (SCLC) to measure the trap density of the perovskite films (Fig. S34 and Table S6). In electron-only devices (ITO/SnO$_2$/perovskite/PCBM/Ag), the trap density drops from 2.79×10^{15} cm^{-3} for the SnO$_2$/PVK device to 1.59×10^{15} cm^{-3} for the SnO$_2$/BNH$_6$/PVK device. In hole-only devices (ITO/PEDOT:PSS/perovskite/Spiro-OMeTAD/Au, the trap densities are reduced from 1.77×10^{15} cm^{-3} for the PVK/Spiro device to 1.29×10^{15} cm^{-3} for the PVK/BNH$_6$/Spiro device. These results confirm that BNH$_6$ all-in-one modification effectively reduces the trap density in perovskites, which is crucial for minimizing nonradiative recombination and improving device performance. Electrical impedance spectroscopy (EIS) results (Fig. S35 and Table S7) further demonstrate that the target device shows larger recombination resistance (R$_{rec}$), suggesting the charge recombination was greatly suppressed with BNH$_6$ all-in-one modification. This is further corroborated by transient photovoltage (TPV) measurement (Fig. S36), where the lifetime of the target device increases to 69.57 μs compared to 57.72 μs for the control device, which reflects the efficiency of BNH$_6$ treatment. Capacitance–voltage ($C-V$) measurement (Fig. S37) shows that the built-in electric field (V_{bi}) increases from 1.01 to 1.09 V with BNH$_6$ modification. The enhanced V_{bi} promotes better charge separation and carrier transport, contributing to the improved V_{oc} and FF in PSCs. Besides, the V_{oc} variation of PSCs under different light intensities shows that the slope reduced from 1.71 k_BT/q for the control device to 1.43 k_BT/q for the target device (Fig. 6f). The lower slope value of the target device indicates a decrease in trap-assisted recombination in PSCs, further supporting the effectiveness of BNH$_6$ in enhancing charge transport and device performance.

The unencapsulated devices under thermal conditions and illumination were evaluated according to the Organic Photovoltaic Stability (ISOS) protocols [61]. Devices aged under thermal stress (65 ± 3 °C, N$_2$ atmosphere) were investigated to monitor the heat stability (ISOS-T-1, Fig. 6g). After continuous heating for around 800 h, the target devices still maintain 84% of the initial PCE, which is remarkably higher than that of the control devices (53%). Furthermore, the light stability was investigated under continuous white LED illumination (100 mV cm^{-2}) in N$_2$ atmosphere for 500 h (ISOS-L-1, Fig. 6h). The target devices preserve 93% of the initial PCE, which is higher than the 75% for the control devices. Meanwhile, the heat and light stability were further researched by XRD to track the degradation of the control and target films (Fig. S38). The control film exhibits distinct degradation after 500 h, as evidenced by the increased intensity of PbI$_2$ peak and the appearance of δ-FAPbI$_3$ peak, whereas the target film shows lower intensity of PbI$_2$ peak and no obvious undesired peaks. In addition, we have evaluated the stability of the unencapsulated devices under ambient air conditions (50–60% RH, 25 °C) (ISOS-D-1, Fig. S39). After 500 h, the control device retained only 85% of the initial PCE, whereas the target device maintained 96% of the initial PCE. These results further demonstrate the effectiveness of the all-in-one modification strategy under more practical conditions.

The operational stability of PSCs was also examined by maximum power point tracking (MPPT) under AM 1.5 G illumination at 25 ± 3 °C with N$_2$ atmosphere (ISOS-L-1, Fig. 6i). After continuous monitoring for 500 h, the target device displays outstanding stability, maintaining 90% of the initial PCE, while the control device only maintains 51% of the initial PCE after 200 h. It suggests that the defects caused by ion migration and organic component volatilization in the target device have been significantly suppressed. To further validate the stability of BNH$_6$, we conducted chemical stability tests on both BNH$_6$ powders and SnO$_2$/BNH$_6$ films under accelerated aging conditions (AM 1.5 G illumination at 25 ± 3 °C with N$_2$ atmosphere, 7 days), as shown in Figs. S40 and S41. The results demonstrate excellent chemical stability, with no significant changes observed in the characteristic signals after aging. These findings confirm that the incorporation of BNH$_6$ does not induce chemical or electrical degradation. Moreover, as shown in Fig. S42, the contact angle for the control film is 53.8°, which increases to 75.9° for the target film, implying the improved hydrophobicity of perovskite film. These results

strongly indicate that the PSCs exhibit improved device performance via BNH_6 all-in-one modification.

4 Conclusion

In summary, an all-in-one modification strategy was proposed by introducing the multifunctional complex BNH_6 to simultaneously address critical challenges at both the buried and upper interfaces of perovskite film. This approach enables BNH_6 to uniquely realize dual-interfacial defect passivation and iodide oxidation suppression by interacting with SnO_2 through hydrolysis, coordinating with Pb^{2+} and inhibiting the oxidation of I^-. These synergistic features enhance perovskite film quality, lead to better energy level alignment, reduce defects, and extend carrier lifetime. As a result, the BNH_6 all-in-one modification strategy significantly improves the PCE to 26.43%. Furthermore, the BNH_6-modified devices exhibit enhanced operational stability, preserving 90% of the initial PCE after continuous tracking for 500 h, a bright contrast to 51% of the control device for 200 h. Thus, the all-in-one strategy streamlines device fabrication by eliminating the need for separate interface treatments, offering a scalable and practical pathway toward high-performance perovskite photovoltaics for practical applications.

Author Contributions Jiaxin Ma: Investigation, original draft writing. Cong shao: Investigation, visualization. Yirong Wang, Guosheng Niu, Kaiyi Yang, Yao Zhao, Fuyi Wang: Conceptualization. Zongxiu Nie, Jizheng Wang: Funding acquisition, review, supervision.

Declarations

References

1. N.J. Jeon, J.H. Noh, W.S. Yang, Y.C. Kim, S. Ryu et al., Compositional engineering of perovskite materials for high-performance solar cells. Nature **517**(7535), 476–480 (2015). https://doi.org/10.1038/nature14133

2. M.M. Lee, J. Teuscher, T. Miyasaka, T.N. Murakami, H.J. Snaith, Efficient hybrid solar cells based on meso-superstructured organometal halide perovskites. Science **338**(6107), 643–647 (2012). https://doi.org/10.1126/science.1228604

3. J. Burschka, N. Pellet, S.-J. Moon, R. Humphry-Baker, P. Gao et al., Sequential deposition as a route to high-performance perovskite-sensitized solar cells. Nature **499**(7458), 316–319 (2013). https://doi.org/10.1038/nature12340

4. M. Liu, M.B. Johnston, H.J. Snaith, Efficient planar heterojunction perovskite solar cells by vapour deposition. Nature **501**(7467), 395–398 (2013). https://doi.org/10.1038/nature12509

5. M.A. Green, A. Ho-Baillie, H.J. Snaith, The emergence of perovskite solar cells. Nat. Photon. **8**(7), 506–514 (2014). https://doi.org/10.1038/nphoton.2014.134

6. H. Min, D.Y. Lee, J. Kim, G. Kim, K.S. Lee et al., Perovskite solar cells with atomically coherent interlayers on SnO_2 electrodes. Nature **598**(7881), 444–450 (2021). https://doi.org/10.1038/s41586-021-03964-8

7. A. Kojima, K. Teshima, Y. Shirai, T. Miyasaka, Organometal halide perovskites as visible-light sensitizers for photovoltaic cells. J. Am. Chem. Soc. **131**(17), 6050–6051 (2009). https://doi.org/10.1021/ja809598r

8. National Renewable Energy Laboratory (NREL). Research Cell Efficiency Records. http://www.nrel.gov/ncpv/images/efficiencychart.jpg (Accessed: June 2025).

9. Y. Zhou, Y. Zhao, Chemical stability and instability of inorganic halide perovskites. Energy Environ. Sci. **12**(5), 1495–1511 (2019). https://doi.org/10.1039/C8EE03559H

10. J.T. Wang, J.M. Ball, E.M. Barea, A. Abate, J.A. Alexander-Webber et al., Low-temperature processed electron collection layers of graphene/TiO_2 nanocomposites in thin film perovskite solar cells. Nano Lett. **14**(2), 724–730 (2014). https://doi.org/10.1021/nl403997a

11. D. Liu, T.L. Kelly, Perovskite solar cells with a planar heterojunction structure prepared using room-temperature solution processing techniques. Nat. Photon. **8**(2), 133–138 (2014). https://doi.org/10.1038/nphoton.2013.342

12. Y. Wu, Q. Wang, Y. Chen, W. Qiu, Q. Peng, Stable perovskite solar cells with 25.17% efficiency enabled by improving crystallization and passivating defects synergistically. Energy Environ. Sci. **15**(11), 4700–4709 (2022). https://doi.org/10.1039/D2EE02277J

13. W. Shao, H. Wang, F. Ye, C. Wang, C. Wang et al., Modulation of nucleation and crystallization in PbI_2 films promoting preferential perovskite orientation growth for efficient solar cells. Energy Environ. Sci. **16**(1), 252–264 (2023). https://doi.org/10.1039/D2EE03342A

14. H. Zhang, Z. Ren, K. Liu, M. Qin, Z. Wu et al., Controllable heterogenous seeding-induced crystallization for high-efficiency FAPbI(3)-based perovskite solar cells over 24. Adv. Mater. **34**(36), e2204366 (2022). https://doi.org/10.1002/adma.202204366

15. P. Shi, Y. Ding, B. Ding, Q. Xing, T. Kodalle et al., Oriented nucleation in formamidinium perovskite for photovoltaics. Nature **620**(7973), 323–327 (2023). https://doi.org/10.1038/s41586-023-06208-z

16. C. Shao, J. He, G. Niu, Y. Dong, K. Yang et al., 2D BA2PbI4 regulating PbI_2 crystallization to induce perovskite growth for efficient solar cells. Small **20**(22), 2309009 (2024). https://doi.org/10.1002/smll.202309009

17. Y. Zhao, F. Ma, Z. Qu, S. Yu, T. Shen et al., Inactive $(PbI_2)_2RbCl$ stabilizes perovskite films for efficient solar cells. Science **377**(6605), 531–534 (2022). https://doi.org/10.1126/science.abp8873

18. K. Wojciechowski, S.D. Stranks, A. Abate, G. Sadoughi, A. Sadhanala et al., Heterojunction modification for highly efficient organic–inorganic perovskite solar cells. ACS Nano **8**(12), 12701–12709 (2014). https://doi.org/10.1021/nn505723h

19. L. Zuo, Z. Gu, T. Ye, W. Fu, G. Wu et al., Enhanced photovoltaic performance of $CH_3NH_3PbI_3$ perovskite solar cells through interfacial engineering using self-assembling monolayer. J. Am. Chem. Soc. **137**(7), 2674–2679 (2015). https://doi.org/10.1021/ja512518r

20. J.-W. Lee, Z. Dai, T.-H. Han, C. Choi, S.-Y. Chang et al., 2D perovskite stabilized phase-pure formamidinium perovskite solar cells. Nat. Commun. **9**(1), 3021 (2018). https://doi.org/10.1038/s41467-018-05454-4

21. H. Hysmith, S.Y. Park, J. Yang, A.V. Ievlev, Y. Liu et al., The role of SnO_2 processing on ionic distribution in double-cation–double halide perovskites. ACS Appl. Mater. Interfaces **15**(30), 36856–36865 (2023). https://doi.org/10.1021/acsami.3c03520

22. C. Li, X. Wang, E. Bi, F. Jiang, S.M. Park et al., Rational design of Lewis base molecules for stable and efficient inverted perovskite solar cells. Science **379**(6633), 690–694 (2023). https://doi.org/10.1126/science.ade3970

23. S. You, H. Zeng, Z. Ku, X. Wang, Z. Wang et al., Multifunctional polymer-regulated SnO_2 nanocrystals enhance interface contact for efficient and stable planar perovskite solar cells. Adv. Mater. **32**(43), 2003990 (2020). https://doi.org/10.1002/adma.202003990

24. T. Duan, S. You, M. Chen, W. Yu, Y. Li et al., Chiral-structured heterointerfaces enable durable perovskite solar cells.

25. S. You, F.T. Eickemeyer, J. Gao, J.-H. Yum, X. Zheng et al., Bifunctional hole-shuttle molecule for improved interfacial energy level alignment and defect passivation in perovskite solar cells. Nat. Energy **8**(5), 515–525 (2023). https://doi.org/10.1038/s41560-023-01249-0

26. H. Zhu, B. Shao, Z. Shen, S. You, J. Yin et al., *In situ* energetics modulation enables high-efficiency and stable inverted perovskite solar cells. Nat. Photon. **19**(1), 28–35 (2025). https://doi.org/10.1038/s41566-024-01542-8

27. S. You, H. Zhu, Z. Shen, X. Wang, B. Shao et al., C(60)-based ionic salt electron shuttle for high-performance inverted perovskite solar modules. Science **388**(6750), 964–968 (2025). https://doi.org/10.1126/science.adv4701

28. W. Xiang, Y. Gao, B. Yuan, S. Xiao, R. Wu et al., Surface-deprotonated ultra-small SnO_2 quantum dots for high-performance perovskite solar cells. Energy Environ. Sci. **18**(1), 406–417 (2025). https://doi.org/10.1039/d4ee03193h

29. S. Xiao, J. Gao, B. Ding, B. Yuan, Y. Gao et al., Multi-hydroxyl and chloric buried interface bridges enable synergistically high-efficiency perovskite solar cells. Small **21**(17), 2500174 (2025). https://doi.org/10.1002/smll.202500174

30. R. Wu, B. Ding, S. Xiao, W. Xiang, Y. Gao et al., Eco-friendly small molecule with polyhydroxyl ketone as buried interface *chelator* for enhanced carrier dynamics toward high-performance perovskite solar cells. Sci. China Mater. **68**(4), 1249–1258 (2025). https://doi.org/10.1007/s40843-024-3228-1

31. Z. Wang, C. Shi, Z. Wang, L. Xiao, T. Wu et al., Solution-processed $Fe_{2-x}Mg_xO_3$ ternary oxides for interface passivation in efficient perovskite solar cells. Chem. Eng. J. **441**, 136118 (2022). https://doi.org/10.1016/j.cej.2022.136118

32. Z. Yi, X. Li, B. Xiao, Q. Jiang, Y. Luo et al., Dual-interface engineering induced by silane coupling agents with different functional groups constructing high-performance flexible perovskite solar cells. Chem. Eng. J. **469**, 143790 (2023). https://doi.org/10.1016/j.cej.2023.143790

33. Y. Zheng, C. Tian, X. Wu, A. Sun, R. Zhuang et al., Dual-interface modification for inverted methylammonium-free perovskite solar cells of 25.35% efficiency with balanced crystallization. Adv. Energy Mater. **14**(20), 2304486 (2024). https://doi.org/10.1002/aenm.202304486

34. X. Gu, W. Xiang, Q. Tian, S. Liu, Rational surface-defect control *via* designed passivation for high-efficiency inorganic perovskite solar cells. Angew. Chem. Int. Ed. **60**(43), 23164–23170 (2021). https://doi.org/10.1002/anie.202109724

35. L. Wang, H. Zhou, J. Hu, B. Huang, M. Sun et al., A Eu(3+)-Eu(2+) ion redox shuttle imparts operational durability to Pb-I perovskite solar cells. Science **363**(6424), 265–270 (2019). https://doi.org/10.1126/science.aau5701

36. Z. Xiao, Y. Yuan, Y. Shao, Q. Wang, Q. Dong et al., Giant switchable photovoltaic effect in organometal trihalide perovskite devices. Nat. Mater. **14**(2), 193–198 (2015). https://doi.org/10.1038/nmat4150

37. C. Eames, J.M. Frost, P.R.F. Barnes, B.C. O'Regan, A. Walsh et al., Ionic transport in hybrid lead iodide perovskite

solar cells. Nat. Commun. **6**, 7497 (2015). https://doi.org/10.1038/ncomms8497

38. S. Chen, X. Xiao, H. Gu, J. Huang, Iodine reduction for reproducible and high-performance perovskite solar cells and modules. Sci. Adv. **7**(10), eabe8130 (2021). https://doi.org/10.1126/sciadv.abe8130

39. N. Wu, T. Yang, Z. Wang, Y. Wu, Y. Wang et al., Stabilizing precursor solution and controlling crystallization kinetics simultaneously for high-performance perovskite solar cells. Adv. Mater. **35**(44), 2304809 (2023). https://doi.org/10.1002/adma.202304809

40. H.-L. Jiang, Q. Xu, Catalytic hydrolysis of ammonia borane for chemical hydrogen storage. Catal. Today **170**(1), 56–63 (2011). https://doi.org/10.1016/j.cattod.2010.09.019

41. K.K. Banger, Y. Yamashita, K. Mori, R.L. Peterson, T. Leedham et al., Low-temperature, high-performance solution-processed metal oxide thin-film transistors formed by a 'sol–gel on chip' process. Nat. Mater. **10**(1), 45–50 (2011). https://doi.org/10.1038/nmat2914

42. J. Liu, S. Li, S. Liu, Y. Chu, T. Ye et al., Oxygen vacancy management for high-temperature mesoporous SnO_2 electron transport layers in printable perovskite solar cells. Angew. Chem. Int. Ed. **61**(26), e202202012 (2022). https://doi.org/10.1002/anie.202202012

43. Z. Zheng, F. Li, J. Gong, Y. Ma, J. Gu et al., Pre-buried additive for cross-layer modification in flexible perovskite solar cells with efficiency exceeding 22. Adv. Mater. **34**(21), e2109879 (2022). https://doi.org/10.1002/adma.202109879

44. C. Gong, H. Li, Z. Xu, Y. Li, H. Wang et al., Efficient and stable inverted perovskite solar cells enabled by homogenized PCBM with enhanced electron transport. Nat. Commun. **15**(1), 9154 (2024). https://doi.org/10.1038/s41467-024-53283-5

45. F. Li, X. Deng, Z. Shi, S. Wu, Z. Zeng et al., Hydrogen-bond-bridged intermediate for perovskite solar cells with enhanced efficiency and stability. Nat. Photon. **17**(6), 478–484 (2023). https://doi.org/10.1038/s41566-023-01180-6

46. Y. Lu, H. Zhu, S. Tan, R. Zhang, M.-C. Shih et al., Stabilization of organic cations in lead halide perovskite solar cells using phosphine oxides derivatives. J. Am. Chem. Soc. **146**(32), 22387–22395 (2024). https://doi.org/10.1021/jacs.4c05398

47. M. Li, R. Sun, J. Chang, J. Dong, Q. Tian et al., Oriented crystallization of FA-based perovskite *via* hydrogen-bonded polymer network for efficient and stable solar cells. Nat. Commun. **14**(1), 573 (2023). https://doi.org/10.1038/s41467-023-36224-6

48. B. Yu, K. Wang, Y. Sun, H. Yu, Minimizing buried interface energy losses with post-assembled chelating molecular bridges for high-performance and stable inverted perovskite solar cells. Adv. Mater. **37**(14), 2500708 (2025). https://doi.org/10.1002/adma.202500708

49. Y. Wang, Y. Meng, C. Liu, R. Cao, B. Han et al., Utilizing electrostatic dynamic bonds in zwitterion elastomer for self-curing of flexible perovskite solar cells. Joule **8**(4), 1120–1141 (2024). https://doi.org/10.1016/j.joule.2024.01.021

50. T. Huang, S. Tan, S. Nuryyeva, I. Yavuz, F. Babbe et al., Performance-limiting formation dynamics in mixed-halide perovskites. Sci. Adv. **7**(46), eabj1799 (2021). https://doi.org/10.1126/sciadv.abj1799

51. K. Wu, A. Bera, C. Ma, Y. Du, Y. Yang et al., Temperature-dependent excitonic photoluminescence of hybrid organometal halide perovskite films. Phys. Chem. Chem. Phys. **16**(41), 22476–22481 (2014). https://doi.org/10.1039/c4cp03573a

52. G. Xing, N. Mathews, S.S. Lim, N. Yantara, X. Liu et al., Low-temperature solution-processed wavelength-tunable perovskites for lasing. Nat. Mater. **13**(5), 476–480 (2014). https://doi.org/10.1038/nmat3911

53. Y. Gao, F. Ren, D. Sun, S. Li, G. Zheng et al., Elimination of unstable residual lead iodide near the buried interface for the stability improvement of perovskite solar cells. Energy Environ. Sci. **16**(5), 2295–2303 (2023). https://doi.org/10.1039/D3EE00293D

54. J. Park, J. Kim, H.-S. Yun, M.J. Paik, E. Noh et al., Controlled growth of perovskite layers with volatile alkylammonium chlorides. Nature **616**(7958), 724–730 (2023). https://doi.org/10.1038/s41586-023-05825-y

55. R. Wang, J. Xue, K.-L. Wang, Z.-K. Wang, Y. Luo et al., Constructive molecular configurations for surface-defect passivation of perovskite photovoltaics. Science **366**(6472), 1509–1513 (2019). https://doi.org/10.1126/science.aay9698

56. S. Zhang, H. Si, W. Fan, M. Shi, M. Li et al., Graphdiyne: bridging SnO_2 and perovskite in planar solar cells. Angew. Chem. Int. Ed. **59**(28), 11573–11582 (2020). https://doi.org/10.1002/anie.202003502

57. Z. Liang, Y. Zhang, H. Xu, W. Chen, B. Liu et al., Homogenizing out-of-plane cation composition in perovskite solar cells. Nature **624**(7992), 557–563 (2023). https://doi.org/10.1038/s41586-023-06784-0

58. R. Chen, J. Wang, Z. Liu, F. Ren, S. Liu et al., Reduction of bulk and surface defects in inverted methylammonium- and bromide-free formamidinium perovskite solar cells. Nat. Energy **8**(8), 839–849 (2023). https://doi.org/10.1038/s41560-023-01288-7

59. L. Luo, H. Zeng, Z. Wang, M. Li, S. You et al., Stabilization of 3D/2D perovskite heterostructures *via* inhibition of ion diffusion by cross-linked polymers for solar cells with improved performance. Nat. Energy **8**(3), 294–303 (2023). https://doi.org/10.1038/s41560-023-01205-y

60. Z. Shen, Q. Han, X. Luo, Y. Shen, Y. Wang et al., Efficient and stable perovskite solar cells with regulated depletion region. Nat. Photon. **18**(5), 450–457 (2024). https://doi.org/10.1038/s41566-024-01383-5

61. M.V. Khenkin, E.A. Katz, A. Abate, G. Bardizza, J.J. Berry et al., Consensus statement for stability assessment and reporting for perovskite photovoltaics based on ISOS procedures. Nat. Energy **5**(1), 35–49 (2020). https://doi.org/10.1038/s41560-019-0529-5